npj | Quantum Materials

www.nature.com/npjquantmats

ARTICLE OPEN

Check for updates

The relevance of ARPES to high-T_c superconductivity in cuprates

Tianlun Yu[1,2✉], Christian E. Matt[1,3], Federico Bisti[1], Xiaoqiang Wang[1], Thorsten Schmitt[1], Johan Chang[3], Hiroshi Eisaki[4], Donglai Feng[2,5,6✉] and Vladimir N. Strocov[1✉]

Angle-resolved photoemission spectroscopy, visualizing the superconducting gap in **k**-space, plays a pivotal role in research on cuprates and other high-T_c superconducting materials. However, there has always been an imminent doubt whether this technique truly represents the intrinsic bulk spectral function, whose response can be distorted by energy- and **k**-dependence of the photoexcitation matrix element, and by a small photoelectron escape depth of few surface atomic layers. Here, we address this fundamental question with soft-X-ray photoemission measurements of the superconducting gap in the paradigm high-T_c cuprate $Bi_2Sr_2CaCu_2O_8$. We vary the matrix element by spanning a dense **k**-space grid, formed by the lattice superstructure, and the probing depth by changing the emission angle. The measured gap appears independent of the matrix element effects, probing depth or photoexcitation energy. This fact proves the relevance of photoemission studies for the bulk superconductivity in $Bi_2Sr_2CaCu_2O_8$, and calls for similar verification experiments on other high-T_c compounds, in particular more three-dimensional ones. $Bi_2Sr_2CaCu_2O_8$ shows an anomalously fast decay of the coherent spectral weight with photon energy, tracing back to strong electron–phonon interaction or relaxation of the lattice coherence.

npj Quantum Materials (2020)5:46 ; https://doi.org/10.1038/s41535-020-0251-3

INTRODUCTION

Since the discovery of high-temperature superconductors (HTSCs) and angle-resolved photoemission spectroscopy (ARPES) has been playing a pivotal role in the research towards the exact mechanisms of this phenomenon[1]. These studies are based on the assumption that the ARPES spectra directly represent the one-electron spectral function $A(\omega, \mathbf{k})$, essentially neglecting matrix element (ME) effects. However, the latter can dramatically depend on energy and **k**, distorting the signature of the true $A(\omega, \mathbf{k})$. Throughout the immensity of ARPES studies, in particular on cuprate HTSCs, most works interpreted the data in terms of $A(\omega, \mathbf{k})$ without paying much attention to the ME effects. Another question is related to the extreme surface sensitivity of ARPES, whose probing depth in the conventional VUV-ARPES range of photon energy $h\nu$ below ~100 eV hardly exceeds 3–5 Å. A still disputed point is whether the SC gap, observed by VUV-ARPES in this thin surface layer, truly represents the intrinsic superconducting (SC) gap in the bulk. The probing depth of the ARPES experiment can be enhanced by pushing it to the soft-X-ray energy range of few hundreds of eV. In the context of SC materials, soft-X-ray ARPES (SX-ARPES, for a recent review see ref. [2]) has previously been used to disentangle bulk from surface states in pnictide superconductors[3] and, more recently, to probe the three-dimensional (3D) electronic structure of overdoped $La_{2-x}Sr_xCuO_4$ (LSCO)[4,5] and of $Bi_2Sr_2CuO_{6+x}$[6]. However, no SX-ARPES studies have so far addressed the SC gap.

Here, we resolve these two fundamental questions regarding the ME and depth-sensitivity effects on the manifestations of superconductivity in ARPES for the paradigm HTSC cuprate $Bi_2Sr_2CaCu_2O_{8+x}$ (Bi2212). First, we investigate the ME effects by measuring the SC gap through a dense grid of **k**-space locations, naturally created by the incommensurate lattice superstructure (LSS) in Bi2212. Second, we assess the surface vs bulk dependence of the SC gap from its measurements at different emission angles. Third, we analyze the excitation-energy dependence of the coherent spectral intensity in terms of its connection to electron–phonon interaction or the LSS coherence. Our SX-ARPES experiments used the paradigm HTSC system Bi2212 because of the relatively large magnitude of its SC gap compared to the experimental energy resolution our $h\nu$ range. Our work puts forward a perspective and methodology for similar verification experiments on other HTSC materials, clearing the way to understand the true mechanisms of their high-T_c superconductivity without overinterpretation of the ARPES data.

RESULTS

Matrix element effects

We start our analysis of the ME effects in Bi2212 from a recap of its crystallographic structure, whose unit cell is shown in Fig. 1a. A peculiarity of Bi2212 is the setting up of the incommensurate LSS along the *a*-axis with a period $\lambda = 26$ Å ~4.8 a_0 (refs [7,8]) as schematized in Fig. 1b. The corresponding cation displacements, projected onto the *ab*-plane, form replicas of the fundamental reciprocal vectors along one-dimensional lines in **k**-space (Fig. 1d).

This LSS manifests itself in the ARPES spectra as multiple replicas of the fundamental band structure and Fermi surface (FS) displaced by $\mathbf{Q}_{LSS} \sim (1/5,1/5)$[9,10]. First of all, we will investigate the intensity of these replicas as a function of $h\nu$. Figure 2a–c shows the experimental in-plane FS measured through the first Brillouin

[1]Swiss Light Source, Paul Scherrer Institut, CH-5232 Villigen PSI, Switzerland. [2]Advanced Materials Laboratory, State Key Laboratory of Surface Physics and Department of Physics, Fudan University, Shanghai 200433, China. [3]Physik-Institut, Universität Zürich, Winterthurerstrasse 190, CH-8057 Zürich, Switzerland. [4]National Institute of Advanced Industrial Science and Technology (AIST), Tsukuba, Ibaraki 305-8568, Japan. [5]Collaborative Innovation Center of Advanced Microstructures, Nanjing 210093, China. [6]Hefei National Laboratory for Physical Science at Microscale, CAS Center for Excellence in Quantum Information and Quantum Physics, and Department of Physics, University of Science and Technology of China, Hefei 230026, China. ✉email: tianlun.yu@psi.ch; dlfeng@fudan.edu.cn; vladimir.strocov@psi.ch

zone (BZ) at $h\nu = 205$, 314, and 404 eV. We observe that the prominence of the replicas relative to the fundamental FS contours is much enhanced compared to the VUV-ARPES spectra[10], and further increases as a function of $h\nu$ in our soft-X-ray energy range. As the probing depth of the ARPES experiment gradually increases with $h\nu$, this observation manifests an increase of the LSS-induced atomic displacements away from the sample surface (see the "Discussion" later). Interestingly, our data show only the main bands and their replicas at $\mathbf{Q}_{LSS}$ without any noticeable signatures of the shadow bands displaced from the main ones by $\mathbf{Q} = (1/2,1/2)$ (ref. [10]).

The LSS provides a natural grid for dense sampling of **k**-space in the ARPES experiment. Indeed, within the one-step photoemission theory (see, for example, refs [11,12]) the ARPES intensity is found as $I_{\mathbf{K}}^{PE} \propto \langle f|\mathbf{A}\cdot\mathbf{P}|i\rangle|^2$, where $\langle f|$ and $|i\rangle$ are the final- and initial-state wavefunctions coupled through the vector potential **A** of incident electromagnetic field and the momentum operator **p**. High excitation energies allow us to use the free-electron final state $\langle f| = e^{i\mathbf{Kr}}\rangle$, where **K** is the photoelectron momentum with the in-plane component $\mathbf{K}_{\|}$. Neglecting for brevity the experimental geometry and X-ray polarization effects contained in **A**·**p**, the ARPES intensity for given **K** appears as the Fourier transform $I_{\mathbf{K}}^{PE} \propto \left|\langle e^{i\mathbf{Kr}}|i\rangle\right|^2$. Expanding $|i\rangle$ over the LSS' in-plane reciprocal vectors **g** as $|i\rangle = \sum_{\mathbf{g}} C_{\mathbf{k}_{\|}+\mathbf{g}} \exp[i(\mathbf{k}_{\|}+\mathbf{g})\mathbf{r}]$, where $\mathbf{k}_{\|}$ is the $|i\rangle$'s in-plane momentum, we obtain $I_{\mathbf{K}}^{PE} \propto \left|\sum_{\mathbf{g}} C_{\mathbf{k}_{\|}+\mathbf{g}} \left\langle e^{i\mathbf{K}_{\|}\mathbf{r}}|e^{i(\mathbf{k}_{\|}+\mathbf{g})\mathbf{r}}\right\rangle\right|^2$. This expression shows, first, that the orthogonality relation $\left\langle e^{i\mathbf{K}_{\|}\mathbf{r}}|e^{i(\mathbf{k}_{\|}+\mathbf{g})\mathbf{r}}\right\rangle = \delta(\mathbf{K}_{\|}, \mathbf{k}_{\|}+\mathbf{g})$ leaves nonzero $I_{\mathbf{K}}^{PE}$ only when $\mathbf{K}_{\|}$ matches a $\mathbf{k}_{\|}+\mathbf{g}$ harmonics of $|i\rangle$ and, second, that the corresponding ME is determined by the coefficient $C_{\mathbf{k}_{\|}+\mathbf{g}}$ of this harmonic varying with **g** for a detailed evaluation including the out-of-plane dependence of $\langle f|$ and $|i\rangle$ (see refs [13,14]). In our case, this means that the ME effects will vary across the **k**-space grid defined by the LSS. Furthermore, in our case this analysis is facilitated by the use of higher $h\nu$ engaging larger LSS-induced atomic displacements in the bulk of Bi2212 which boost intensity of the LSS-replicas. We will now leverage this idea to verify whether the ME effects, varying along these replicas, affect the SC gap apparent in the ARPES experiment.

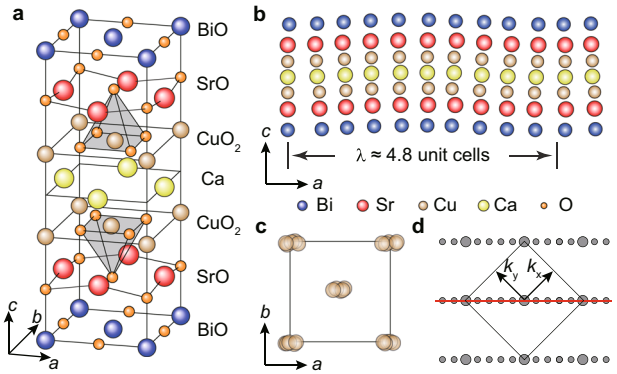

Fig. 1 Sketch of Bi2212's lattice structure. a The upper half of the Bi2212 unit cell. **b** A sketch of the cation displacement projected onto the *ac*-plane. **c** The cation displacements projected onto the *ab*-plane. **d** The superstructure in **k**-space. The conventional basis vectors are shown. The red line indicates the measurement direction of our ARPES experiments.

Our SC gap analysis used the ARPES data acquired at 205 eV, where the coherent spectral component (see below) was the largest. Figure 3a shows the experimental band structure along the **k**-space cut #1, indicated in the FS map in Fig. 2a as #1. These **k**-points have been chosen to avoid the regions of hybridization between the main and replica bands, where the dispersions are distorted[15], and keep the gap large enough in comparison with our experimental resolution. Figure 3b represents this band structure symmetrized relative to Fermi level (E_F) as $I^{PE}(E, \mathbf{k}) = I^{PE}(-E, \mathbf{k})$. Whereas the strict hole–particle symmetry, implying a simultaneous inversion of **k** as $A(\omega, \mathbf{k}-\mathbf{k}_F) = A(-\omega, -\mathbf{k}-\mathbf{k}_F)$, would in our case show confusing discontinuous between the regions centered at $\mathbf{k}_F$ of each replica band, our simplistic symmetrization, albeit not physically rigorous, well serves visualization of the SC gaps through all fundamental and replica bands. These gaps all close below 105 K, as shown in the corresponding Fig. 3c, d. This fact confirms that the observed gaps are the SC ones rather than the pseudogaps[16]. Moreover, the band dispersions at low temperature show a clear bending, characteristic of the formation of the SC gap. Furthermore, Fig. 3e shows the symmetrized

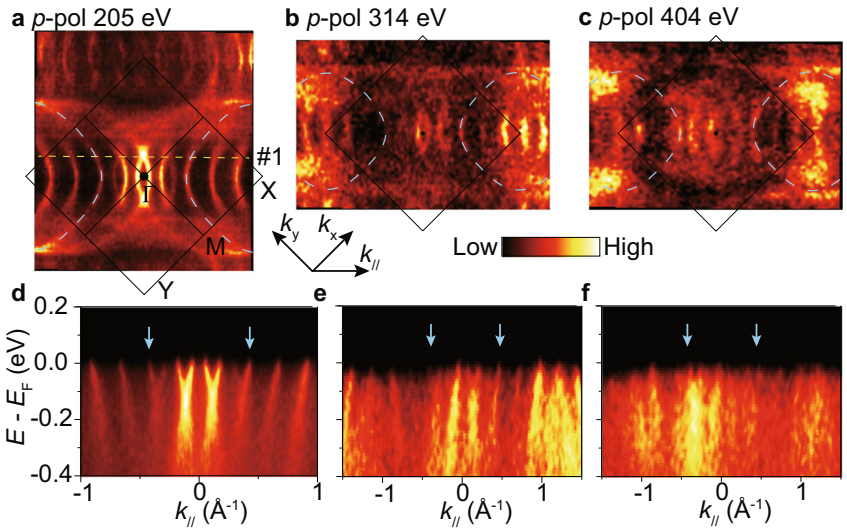

Fig. 2 Experimental in-plane FS in the first BZ. a–c The FS measured at $h\nu = 205$, 314, and 404 eV, respectively. The blue dashed contours indicate the fundamental FS. **d–f** Their corresponding ARPES intensity along XΓX cut (nodal line). The blue arrows indicate the fundamental band dispersions. The replica contours form a dense grid in **k**-space. Their intensity scales up compared to the fundamental contours, manifesting an increase of the LSS-induced atomic displacements into the sample bulk.

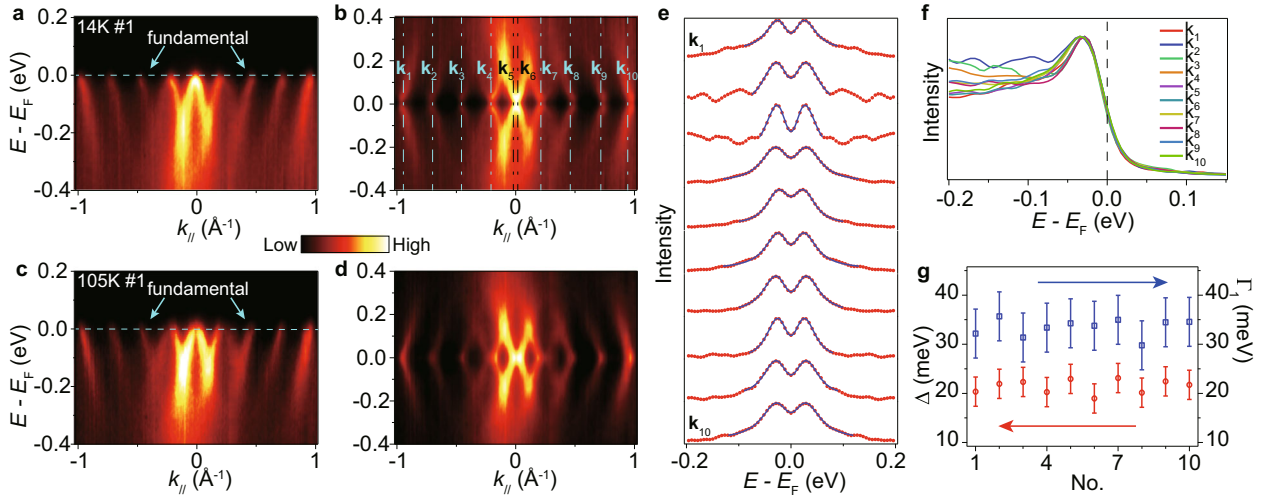

Fig. 3 ARPES data measured at $h\nu = 205$ eV. a ARPES intensity in the SC state along the cut #1 in Fig. 2b. **b**. The corresponding image symmetrized relative to E_F, manifesting the SC gap. The dashed lines $\mathbf{k}_1$ through $\mathbf{k}_{10}$ indicate E_F-crossings for the fundamental bands and their LSS-replicas. **c**, **d** The same measurements at 105 K where the SC gap is absent. **e** Symmetrized EDCs (red) for the SC state, extracted from panel **b** at the **k**-points $\mathbf{k}_1$ through $\mathbf{k}_{10}$ and their fitting (blue) with the SC spectral function. **f** The comparison of the EDCs at $\mathbf{k}_1$ through $\mathbf{k}_{10}$. **g** The magnitude of the SC gap (red) and Γ_1 (blue) derived by fitting (error bars indicated). These SC gap parameters are the same within the experimental accuracy. The error bars are due to the experimental energy resolution.

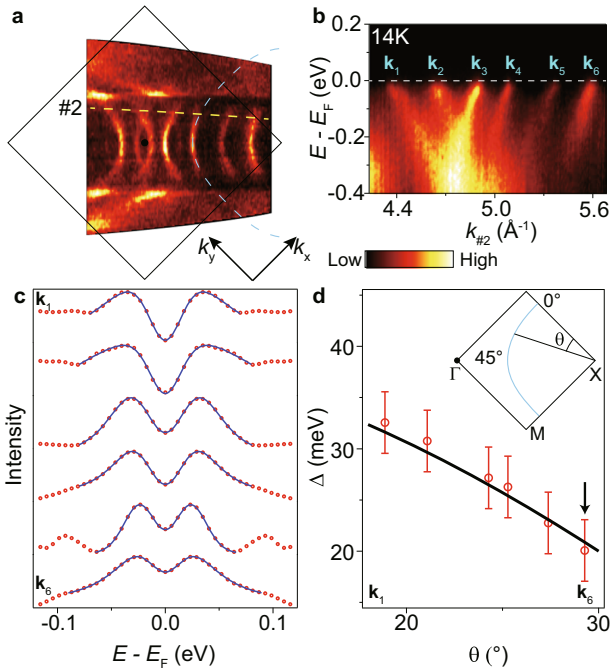

Fig. 4 ARPES data measured at off-normal-emission angles around 47°, corresponding to the (2, −2) BZ. a Experimental in-plane FS measured at $h\nu = 205$ eV, with the blue dashed curve indicating the fundamental FS. **b** ARPES intensity along the cut marked as #2 in panel **a**. $\mathbf{k}_1$ through $\mathbf{k}_6$ indicate the E_F-crossings. **c** Symmetrized EDCs at $\mathbf{k}_1$ through $\mathbf{k}_6$ (red) and their fitting with the SC spectral function (blue). **d** The magnitude of the SC gap derived by fitting with the error bars indicated. The SC gap decreases from 32 meV at $\mathbf{k}_1$ to 20 meV at $\mathbf{k}_6$, in accordance with the gap anisotropy. The experimental points are fitted with the *d*-wave gap function (black line). The arrow indicates $\mathbf{k}_6$ which is equivalent to **k** of the cut #1 through the first BZ (Fig. 3). The same SC gap magnitudes indicate the absence of its depth dependence. The error bars are due to the experimental energy resolution.

energy-distribution curves (EDCs) in the SC state, extracted from Fig. 3b at $\mathbf{k}_1$ through $\mathbf{k}_{10}$. The corresponding values of the SC gap were found by their fitting with the SC spectral function convolved with the energy resolution based on the simplified BCS self-energy $\sum(\mathbf{k},\omega) = -i\Gamma_1 + \Delta^2/[\omega + \varepsilon(\mathbf{k}) + i\Gamma_0]$, where Δ is the SC gap width, Γ_1 is a single-particle scattering rate, $\varepsilon(\mathbf{k})$ then dispersion (with $\varepsilon(\mathbf{k}_F) = 0$), and $i\Gamma_0$ is viewed as the inverse pair lifetime, which should be zero in the SC state[17]. Through the whole grid of our **k**-space locations, we find $\Delta_{SC} = 21 \pm 3$ meV and $\Gamma_1 = 34 \pm 5$ meV (Fig. 3g).

These data show that the SC gap parameters, observed through all **k**-space locations sampled by the LSS, are the same within the experimental accuracy regarding both the gap magnitude and single-particle scattering rate. Furthermore, our experimental gap magnitude is fully consistent with previous VUV-ARPES results[16]. As the ME effects must be different between different **k**-space locations, the observed constant SC gap gives us the sough-for proof of the absence of any significant ME-induced artefacts in its experimental determination by ARPES. We note that STM experiments for Bi2212 have found that the SC gap magnitude slightly (by ~9% of the mean value) differs between different atomic sites[8]. However, this observation does not contradict to our results where the SC gap is measured in **k**-space. Analysis of **k**-dependence of the high-energy dispersion anomalies—so-called waterfalls[16,18–20]—was in our case hindered by overlapping of their spectral signatures coming from different replicas. For the materials without the LSS, the idea to investigate the ME effects by measurements of the SC gap in equivalent **k**-points can be realized, albeit on a coarser **k**-grid, by going through different fundamental-lattice BZs. To the best of our knowledge, however, this idea has not yet been applied to any HTSC system.

Depth dependence of the SC gap

We will now address the question whether the SC gap magnitude is depth-dependent. If so, the surface-sensitive ARPES measurements might yield its values deviating from the bulk transport properties. We have accessed this effect by comparing the above ARPES data measured near the normal emission (NE) with those measured at more grazing emission angles.

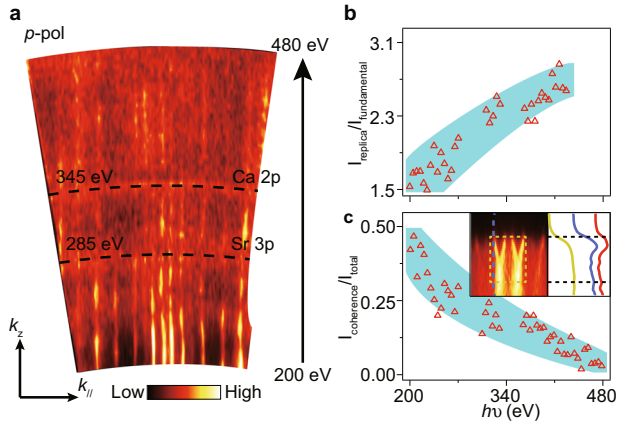

Fig. 5 Photon-energy-dependent ARPES response. a The out-of-plane FS map ($k_{//}$ along the ΓX direction in the BZ). The FS contours are straight as a function of k_z, confirming the 2D character of Bi2212. **b** Intensity ratio of the replica to fundamental FS contours as a function of *hv*. Its increase manifests an increase of the LSS-induced atomic $\int I^{PE}(E,k_{||})dk_{||}$ displacements into the sample depth. **c** Coherent spectral weight. Its fast decrease with *hv* and nearly vanishing above 460 eV suggests mechanisms beyond the conventional DW-picture. The inset illustrates the spectral intensity $\int I^{PE}(E,k_{||})dk_{||}$ (yellow) integrated over the area Ω (dashed yellow rectangle), the EDC (blue) at the blue dashed line and its corresponding I^{coh} component (red).

The experimental off-NE data for the SC state, measured at $hv = 205$ eV around an emission angle of ~47° and corresponding to the (2, −2) BZ, are presented in Fig. 4. Similarly to the normal-emission data, the in-plane FS (Fig. 4a) shows the fundamental and replica contours. Correspondingly, the experimental band structure along the **k**-space cut, marked on the map as #2, shows the E_F-crossings marked $\mathbf{k}_1$ through $\mathbf{k}_6$. The symmetrized EDCs at these points (Fig. 4c) and the results of their fitting (Fig. 4d) show that the SC gap decreases from ~32 meV at $\mathbf{k}_1$ to ~20 meV at $\mathbf{k}_6$. Following the fit with the (simplified) *d*-wave gap function[21] $\Delta_k = \Delta_{max}$ cos (2θ), this decrease manifests the gap anisotropy along our inclined path in **k**-space. Indeed, the previous VUV-ARPES study[16] has shown that in the near-optimal doped Bi2212 the SC gap decreases from its maximal value 35–40 meV, characterizing the pseudogap at the antinodal point, to zero at the nodal point. Our values of the SC gap, going from near the antinodal point ($\mathbf{k}_1$) to the middle between the nodal and antinodal point ($\mathbf{k}_6$), are consistent with this dependence measured at smaller probing depth. Specifically, the gap found at the $\mathbf{k}_6$-point is equal, within the experimental uncertainty, to that found in the equivalent **k**-points $\mathbf{k}_1$–$\mathbf{k}_{10}$ in our near-NE data in Fig. 3. This fact gives us the sought for evidence that the SC gap in Bi2212 is independent of the probing depth. This pattern may however change for other HTSCs, for example, for more 3D compounds from the LSCO[4,5] and YBCO[22] families.

Photon-energy-dependent ARPES response

Finally, we will analyze full *hv*-dependence of the ARPES spectral structure, presented in Fig. 5a as the out-of-plane FS map as a function of $k_{//}$ (along the direction marked on the in-plane FS map in Fig. 2) and *hv* increasing from 200 to 480 eV. The narrow-curved contours around 285 and 345 eV (marked in Fig. 5a) are due to the core level electrons excited by high-order radiation from the beamline. Intensity modulations as a function of *hv* may be connected with the photoemission cross section variations with the final state k_z similar to the known intensity variations between the bonding and antibonding states[23]. The experimental out-of-plane FS map elucidates several important aspects of physics of Bi2212.

First of all, we note that the probing depth of our experiment in the soft-X-ray energy range, which is of the order of 1 nm (ref. [24]), is significantly higher compared to the previous VUV-ARPES studies. However, despite the proportional improvement of k_z-resolution[25], we observe only k_z-independent FS contours. This observation extends not only to the ΓX (nodal) direction in Fig. 5 but also to the ΓM (antinodal) one, where the k_z-dispersion might be more pronounced (not shown here for brevity). This fact confirms the purely two-dimensional (2D) character of Bi2212, contrasting it to other HTSC cuprates such as the LSCO[4,5] and YBCO[22] compounds.

Our second point extends the above analysis of the relative replica to fundamental spectral intensities. Their intensity ratio as a continuous function of *hv*, derived from the data in Fig. 5a, is presented in Fig. 5b. It shows a gradual increase with *hv*, which is consistent with previous works in the VUV region where the replicas appear in general weaker than the main band not only for Bi2212[10,23] but also for other cuprates such as $Bi_2Si_{2-x}La_xCuO$[26]. This phenomenon should be connected with the increase of photoelectron escape depth with energy. Indeed, the universal curve[24] suggests that the escape depth increases from 3–5 Å in the VUV region to 5–10 Å towards 200 eV and further to about 15 Å towards 500 eV. Then the increase of the relative intensity of the replicas identifies an increase of the LSS-induced atomic displacements with the depth into the sample bulk, at least in the CuO-plane second from the surface. This observation is in agreement with the standing-wave photoemission experiments on Bi2212 (ref. [6]). Whereas the absence of reliable data on the exact escape depth in Bi2212 has left as with merely a qualitative conclusion on the depth dependence of the atomic displacements, their quantitative evaluation is calling for grazing-incidence X-ray diffraction experiments.

The third and most intriguing point is the energy dependence of the coherent **k**-dependent spectral weight $I^{coh}(E,\mathbf{k})$. It was evaluated for every ARPES image, constituting the map in Fig. 5a, in an energy window of 200 meV below E_F as $I^{coh}(E,k_{||}) = I(E,k_{||}) - a\int I^{PE}(E,k_{||})dk_{||}$, where the $k_{||}$-integration window Ω around the Γ-point is shown in the inset of Fig. 5c, and *a* is its maximum value leaving $I^{coh}(E,\mathbf{k}) > 0$ throughout Ω (for robustness against the noise, within 95% in the histogram). The $k_{||}$-integrated values of I^{coh} as a function of *hv* are presented in Fig. 5c. The oscillation of this dependence around 260 eV are attributed to the photoemission cross section variation discussed above. Most importantly, the experimental I^{coh} shows an unexpectedly fast decay of the coherent spectral weight with *hv*. This fact is actually seen already in Fig. 2 from the sequence of in-plane FS maps Fig. 2a–c measured with increasing *hv*. To the best of our knowledge, the observed decay of I^{coh} is the fastest among all materials investigated so far by SX-ARPES (see the recent review[2] and the references therein) including the HTSC cuprates of the LSCO[4,5] and YBCO[22] families. We can rule out any significant influence of the sample aging on the observed decay as a function of *hv*, because it was the same when measured in a sequence going from low to high and from high to low *hv*, where the spectra stayed clear and sharp through the whole experimental round. Moreover, our preliminary measurements on overdoped Bi2212 samples have shown the same fast decay of the coherent spectral weight with *hv*.

In general, the decay of I^{coh} is determined by the relation of the de Broglie wavelength of the photoelectrons $\lambda_B = h/p$, where *p* is expressed through their mass *m* and kinetic energy E_k as $p = (2mE_k)^{1/2}$, to the thermal atomic-displacement amplitudes. When upon increase of *hv* or *T* these two become comparable, the dipole selection rules relax and the coherent I^{coh} decays[2,27]. This effect is conventionally described within the Debye–Waller (DW)

model as $I^{coh} = W(T)I^{coh}_{T=0}$, where $W(T) = \exp(-\Delta K^2\langle u^2(T)\rangle)$ is the DW-factor with the momentum transfer $\Delta K \propto \sqrt{h\nu}$ and mean-squared atomic displacements $\langle u^2\rangle$, roughly proportional to T. In our data, however, I^{coh} decays with $h\nu$ much faster compared to the DW-model with any reasonable $<u^2>$ at our working temperature $T \sim 14$ K. Even more intriguing, at $h\nu =$ 205 eV I^{coh} well survives at least up to 105 K (Fig. 3c, d) despite the increase of $h\nu$ to 460 eV and T to 105 K delivers comparable values of the DW-factor.

One of the sources of such dramatic deviations from the DW-model may be recoil effects[28]. Physically, the recoil can be viewed as an emission of phonons back into the crystal lattice by the escaping photoelectrons[29], where the associated atomic displacements will erode I^{coh} similarly to the thermally excited phonons. This effect will progressively increase with $h\nu$ but hardly depend on T, consistent with our experimental results. The prominence of such recoil effects might be related to the known strong electron–phonon interaction in Bi2212, albeit for the valence electrons[30]. Another scenario[9] proposes to relate the anomalous decay of I^{coh} to the LSS' incommensurability. We argue, however, that this phenomenon may be attributed rather to a small coherence length of the LSS. Indeed, STM studies[8,9] have found them irregular, with the spatial phase slipping and meandering on a scale of few hundreds of Å. These atomic displacements will cut down I^{coh} as soon as they become comparable with λ_B. Indeed, whereas the former can be estimated as ±0.4Å [8,9], the quenching of I^{coh} at $h\nu \sim 460$ eV corresponds to a comparable value of ~0.6Å. The quenching is accelerated by the gradual increase of the SX-ARPES probing depth with energy, invoking larger LSS-induced atomic displacements in the deeper atomic layers of Bi2212.

DISCUSSION

We have used SX-ARPES to investigate the SC gap magnitude in Bi2212 as apparent in the photoemission spectra under variation of the ME effects and of the probing depth. The former was varied by measurements of the SC gap over a dense grid of equivalent **k**-points formed by the LSS-replicas of the FS, taking into advantage strengthening of the LSS-induced atomic displacements into the bulk of Bi2212. The latter was varied by changing from a bulk-sensitive experimental geometry near the NE to a more surface-sensitive one at grazing emission angles. Our SX-ARPES experiments have demonstrated that the experimental SC gap is neither affected by the ME effects nor depends on the depth into the sample, and stays fully consistent with the previous VUV-ARPES results. These results clear up the still-existing doubts on the relevance of ARPES as a tool to explore the intrinsic mechanisms of high-T_c superconductivity in Bi2212. In this context, the observed **k**-dependence of the dispersion waterfalls[16,18–20] in Bi2212 is a sign of their (at least partially) extrinsic origin related to the ME effects.

The applicability of ARPES to other HTSC compounds can be verified using the same methodological path. If the LSS is absent, the ME effects can be varied by measurements of the SC gap through different BZs. Furthermore, these effects can be reduced by measurements in the soft-X-ray energy range[2] where free-electron character of the photoemission final states reduces the MEs essentially to atomic photoionization cross sections smoothly varying with energy. High-energy resolution in this energy range requires, however, most advanced synchrotron radiation beamlines. The depth dependence of the SC gap, whose absence for Bi2212 might be connected with the purely 2D character of this compound, can come into play for other more 3D HTSCs such as the cuprates from the LSCO[4,5] and YBCO[22] families. This point also needs verification before using ARPES data to draw valid conclusions about the bulk superconductivity in these materials. Our work puts forward a perspective and methodology for similar verification experiments, clearing the way to understanding the true mechanisms of their high-T_c superconductivity without overinterpretation of the ARPES data.

Our last and equally intriguing point is Bi2212's decay of the coherent spectral weight with $h\nu$, which is much faster even compared to other cuprates. It remains to be explored whether such dramatic deviations from the DW-model hint at recoil effects, invoked by strong electron–phonon interaction in Bi2212, or at small coherence length of the incommensurate LSS.

METHODS

High-quality near-optimal doped Bi2212 ($T_c \sim 91$ K) single crystals were grown by the floating zone method as described elsewhere[9]. SX-ARPES experiments were performed in the $h\nu$ range 200–500 eV at the ADRESS beamline of the Swiss Light Source, Paul Scherrer Institute, Switzerland. The photoelectrons were detected with the analyzer PHOIBOS-150 from SPECS GmbH at an angular resolution of ~0.1°. The combined energy resolution was set to 30–40 meV. The E_F position of the samples was referred to that of a gold foil in electrical contact with the sample. The FS maps were integrated within $E_F \pm 20$ meV. The experiment was performed in vacuum $< 9 \times 10^{-11}$ mbar at a base sample temperature of ~14 K. The samples were cleaved in situ after cooling down.

DATA AVAILABILITY

The dataset supporting the key findings of this study are available at https://doi.org/10.7910/DVN/3OFENZ.

Received: 10 March 2020; Accepted: 22 June 2020;
Published online: 09 July 2020

REFERENCES

1. Damascelli, A., Hussain, Z. & Shen, Z.-X. Angle-resolved photoemission studies of the cuprate superconductors. *Rev. Mod. Phys.* **75**, 473–541 (2003).
2. Strocov, V. N. et al. k-resolved electronic structure of buried heterostructure and impurity systems by soft-X-ray ARPES. *J. Electron Spectrosc. Relat. Phenom.* **236**, 1–8 (2019).
3. Razzoli, E. et al. Bulk electronic structure of superconducting $LaRu_2P_2$ single crystals measured by soft-X-ray angle-resolved photoemission spectroscopy. *Phys. Rev. Lett.* **108**, 257005 (2012).
4. Horio, M. et al. Three-dimensional fermi surface of overdoped La-based cuprates. *Phys. Rev. Lett.* **121**, 077004 (2018).
5. Matt, C. E. et al. Direct observation of orbital hybridisation in a cuprate superconductor. *Nat. Commun.* **9**, 972 (2018).
6. Kramer, K. P. et al. Band structure of overdoped cuprate superconductors: density functional theory matching experiments. *Phys. Rev. B* **99**, 224509 (2019).
7. He, Y., Graser, S., Hirschfeld, P. J. & Cheng, H.-P. Supermodulation in the atomic structure of the superconductor $Bi_2Sr_2CaCu_2O_{8+x}$ from ab initio calculations. *Phys. Rev. B* **77**, 220507 (2008).
8. Slezak, J. A. et al. Imaging the impact on cuprate superconductivity of varying the interatomic distances within individual crystal unit cells. *Proc. Natl Acad. Sci.* **105**, 3203–3208 (2008).
9. Kuo, C.-T. et al. Atomic-layer-resolved composition and electronic structure of the cuprate $Bi_2Sr_2CaCu_2O_{8+\delta}$ from soft x-ray standing-wave photoemission. *Phys. Rev. B* **98**, 155133 (2018).
10. Mans, A. et al. Experimental proof of a structural origin for the shadow fermi surface of $Bi_2Sr_2CaCu_2O_{8+\delta}$. *Phys. Rev. Lett.* **96**, 107007 (2006).
11. Feibelman, P. J. & Eastman, D. E. Photoemission spectroscopy—correspondence between quantum theory and experimental phenomenology. *Phys. Rev. B* **10**, 4932–4947 (1974).
12. Krasovskii, E. E. & Schattke, W. Angle-resolved photoemission from surface states. *Phys. Rev. Lett.* **93**, 027601 (2004).
13. Strocov, V. N., Starnberg, H. I. & Nilsson, P. O. Excited-state bands of Cu determined by VLEED band fitting and their implications for photoemission. *Phys. Rev. B* **56**, 1717–1725 (1997).
14. Strocov, V. N. Photoemission response of 2D electron states. *J. Electron Spectrosc. Relat. Phenom.* **229**, 100–107 (2018).
15. Gao, Q. et al. Selective hybridization between the main band and the superstructure band in the $Bi_2Sr_2CaCu_2O_{8+\delta}$ superconductor. *Phys. Rev. B* **101**, 014513 (2020).
16. Vishik, I. M. et al. ARPES studies of cuprate fermiology: superconductivity, pseudogap and quasiparticle dynamics. *N. J. Phys.* **12**, 105008 (2010).

17. Norman, M. R., Randeria, M., Ding, H. & Campuzano, J. C. Phenomenology of the low-energy spectral function in high-Tc superconductors. *Phys. Rev. B* **57**, R11093–R11096 (1998).
18. Inosov, D. S. et al. Momentum and energy dependence of the anomalous high-energy dispersion in the electronic structure of high temperature superconductors. *Phys. Rev. Lett.* **99**, 237002 (2007).
19. Chang, J. et al. When low- and high-energy electronic responses meet in cuprate superconductors. *Phys. Rev. B* **75**, 224508 (2007).
20. Inosov, D. S. et al. Excitation energy map of high-energy dispersion anomalies in cuprates. *Phys. Rev. B* **77**, 212504 (2008).
21. Mesot, J. et al. Superconducting gap anisotropy and quasiparticle interactions: a doping dependent photoemission study. *Phys. Rev. Lett.* **83**, 840–843 (1999).
22. Zabolotnyy, V. B. et al. Pseudogap in the chain states of $YBa_2Cu_3O_{6.6}$. *Phys. Rev. B* **85**, 064507 (2012).
23. Chuang, Y.-D. et al. Bilayer splitting and coherence effects in optimal and underdoped $Bi_2Sr_2CaCu_2O_{8+\delta}$. *Phys. Rev. B* **69**, 094515 (2004).
24. Seah, M. P. & Dench, W. A. Quantitative electron spectroscopy of surfaces: a standard data base for electron inelastic mean free paths in solids. *Surf. Interface Anal.* **1**, 2–11 (1979).
25. Strocov, V. N., Claessen, R. & Blaha, P. Origin of photoemission final-state effects in $Bi_2Sr_2CaCu_2O_8$ by very-low-energy electron diffraction. *Phys. Rev. B* **68**, 144509 (2003).
26. King, P. D. C. et al. Structural origin of apparent fermi surface pockets in angle-resolved photoemission of $Bi_2Sr_{2-x}La_xCuO_{6+\delta}$. *Phys. Rev. Lett.* **106**, 127005 (2011).
27. Braun, J. et al. Exploring the XPS limit in soft and hard x-ray angle-resolved photoemission using a temperature-dependent one-step theory. *Phys. Rev. B* **88**, 205409 (2013).
28. Suga, S. et al. Do all nuclei recoil on photoemission in compounds? *N. J. Phys.* **11**, 073025 (2009).
29. Hofmann, P. et al. Unexpected surface sensitivity at high energies in angle-resolved photoemission. *Phys. Rev. B* **66**, 245422 (2002).
30. Grimaldi, C., Pietronero, L. & Strässler, S. Nonadiabatic superconductivity: electron-phonon interaction beyond Migdal's theorem. *Phys. Rev. Lett.* **75**, 1158–1161 (1995).

ACKNOWLEDGEMENTS

We thank A. Kordyuk, M. Shi, and N.B.M. Schroeter for critical reading of the manuscript and valuable advice, and L. Nue for skillful engineering support.

AUTHOR CONTRIBUTIONS

V.N.S. and T.Y. at the Swiss Light Source and D.F. at Fudan University conceived the SX-ARPES research on Bi2212. T.Y. performed the actual SX-ARPES experiments, and C.E.M. and F.B. pilot experiments supported by V.N.S., X.W., and T.S. T.Y. processed the data supported by V.N.S. H.E. grew the samples. All authors discussed the results, interpretations, and scientific concepts. T.Y. and V.N.S. wrote the manuscript supported by D.F., J.C., and all other authors.

COMPETING INTERESTS

The authors declare no competing interests.

ADDITIONAL INFORMATION

Correspondence and requests for materials should be addressed to T.Y., D.F. or V.N.S.

Reprints and permission information is available at http://www.nature.com/reprints

Publisher's note Springer Nature remains neutral with regard to jurisdictional claims in published maps and institutional affiliations.

Open Access This article is licensed under a Creative Commons Attribution 4.0 International License, which permits use, sharing, adaptation, distribution and reproduction in any medium or format, as long as you give appropriate credit to the original author(s) and the source, provide a link to the Creative Commons license, and indicate if changes were made. The images or other third party material in this article are included in the article's Creative Commons license, unless indicated otherwise in a credit line to the material. If material is not included in the article's Creative Commons license and your intended use is not permitted by statutory regulation or exceeds the permitted use, you will need to obtain permission directly from the copyright holder. To view a copy of this license, visit http://creativecommons.org/licenses/by/4.0/.

© The Author(s) 2020